Supporting Information for

Layer Number Dependence of MoS_2 Photoconductivity Using Photocurrent Spectral Atomic Force Microscopic Imaging

Youngwoo Son[†,‡], Qing Hua Wang[†,∥,‡], Joel A. Paulson[†], Chih-Jen Shih[†,#], Ananth G. Rajan[†], Kevin Tvrdy[§], Sojin Kim[†], Bassam Alfeeli[⊥,∇], Richard D. Braatz[†], and Michael S. Strano[†,]*

† Department of Chemical Engineering, Massachusetts Institute of Technology, Cambridge, Massachusetts 02139, United States

§ Department of Chemistry and Biochemistry, University of Colorado at Colorado Springs, Colorado Springs, Colorado 80918, United States

⊥ KUWAIT-MIT Center for Natural Resources and Environment, Massachusetts 02139, United States

∇ Nanotechnology and Advanced Materials Program, Energy & Building Research Center, Kuwait Institute for Scientific Research, Safat, 13109, Kuwait

‡ These authors contributed equally to this work.

Present address: Institute for Chemical and Bioengineering, ETH Zurich, HCI E 133, Vladimir-Prelog-Weg 1, CH-8093 Zurich, Switzerland

∥ Present address: Materials Science and Engineering, School of Engineering of Matter, Transport and Energy, Arizona State University, Tempe, Arizona 85287, United States

* Author to whom all correspondence should be addressed. Email: strano@mit.edu

Contents:

1. Estimation of effective contact area (A_e)

During conductive AFM (C-AFM) imaging, determining the tip loading force and estimating the effective current emission area are necessary for high spatial resolution and proper analysis of experimentally obtained *I-V* characteristics while not damaging the sample under investigation. In our C-AFM experimental setup the nanoscale contacts are formed between the conductive tip and MoS_2 nanosheet. We used the Hertz contact theory[1-3] to estimate the effective contact area. The tip is assumed to be an elastic sphere and the underlying sample surface is assumed to be flat to describe the contact formed between the tip and MoS_2 nanosheets, as schematically illustrated in Figure S1. We assume that the carrier injection is concentrated in this region where the tip and substrate are in contact, and the field contribution from the side part diverges at MoS_2 surface. The contact area radius, *a*, is calculated by:

$$a = \left[\frac{3RF}{4} \left(\frac{1-\nu_1^2}{E_1} + \frac{1-\nu_2^2}{E_2} \right) \right]^{1/3} \tag{S1}$$

where *R* denotes the tip radius, *F* the contact force, $\nu_{1,2}$ the Poisson ratios, and $E_{1,2}$ the elastic moduli of MoS_2 flakes and the conductive tip.

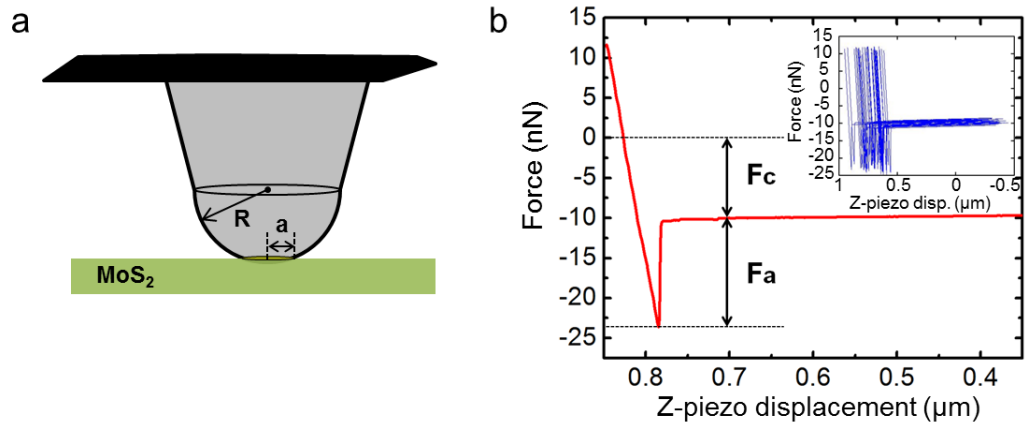

Figure S1. (a) Schematic illustration of the contact between the conductive tip and MoS_2 flake surface. *R* denotes the tip radius and *a* the contact area radius. (b) Representative force-displacement (*F-D*) curve in which F_c represents the instrumental deflection set-point force and F_a the additional force between the tip and the sample surface. Inset shows a series of *F-D* curves taken before and after each of the current images.

Figure S1b shows a representative force-displacement (*F-D*) curve of the measurements where retraction force is presented in this figure for clarity. The contact force, *F*, is the sum of the instrument deflection set point force (F_c) and additional adhesive force (F_a) between the tip and the flake, which was maintained at around moderate value of 20 nN to ensure reliable current measurements while not physically damaging the sample surface or tip coating and preserving high spatial resolution during imaging in order to obtain nanoscale local electronic properties.[4] The inset in Figure S1b shows a series of *F-D* curves that were measured before and after each of about 20 image scans for Figures 2e-l and S3. No noticeable change in the physical interaction between the tip and the sample was observed throughout all the experiments, which suggests the C-AFM measurements were reliable and not deteriorated by tip degradation or oxidation. Previously reported elastic moduli and Poisson ratios of

platinum, iridium[5] and MoS_2[6, 7] are provided in Table 1 and were used to calculate the effective contact area, $A_e = \pi a^2$, which ranges from 3.88nm^2 to 6.43nm^2.

Table S1. Elastic moduli, Poisson ratios and calculated effective contact area

Material	Elastic modulus (GPa)	Poisson ratio	A_e (F=20-25nN) (nm^2)
MoS_2	350	0.125	3.88 – 6.43
Platinum	170	0.39	
Iridium	528	0.26	

2. Calculation of ideality factor and barrier height

The barrier height Φ_B can be calculated from the saturation current I_0 (5.7×10^{-13} A) that was obtained by fitting the data in the reverse bias regime to the thermionic emission model.[8] The Richardson constant (A^*) is expressed as follows:

$$A^* = \frac{4\pi q m k_B^2}{h^3} \tag{S2}$$

where k_B denotes the Boltzmann constant, q the electronic charge, m the electron mass, and h the Planck constant. The barrier height can then be calculated as

$$\Phi_B = \frac{k_B T}{q} \ln\left(\frac{A^* A T^2}{I_0}\right) = 1.2\text{eV}$$

The ideality factor η can be calculated from the slope of the linear region shown in Figure S2.

$$\eta = \frac{q}{k_B T}\frac{dV}{d(\ln I)} = 5.6$$

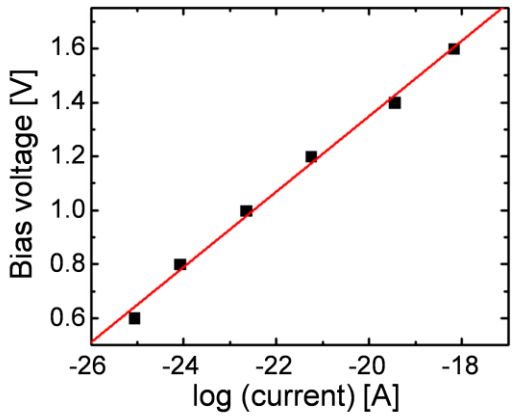

Figure S2. A semilogarithmic plot of bias voltage as a function of log (current). A red straight line indicates a linear fit to the data.

3. Layer number dependence of the barrier heights

Figure S3 shows the extracted barrier heights (Φ_B) by fitting to the FN-tunneling model as a function of layer number from the MoS_2 flake shown in Figure 2 in the main text. As layer number increases from 1L to 4L Φ_B increases gradually from 0.61 eV to 0.69 eV in a nonlinear fashion where the rate of increase is slowed that Φ_B of 3L reached close to that of 4L.

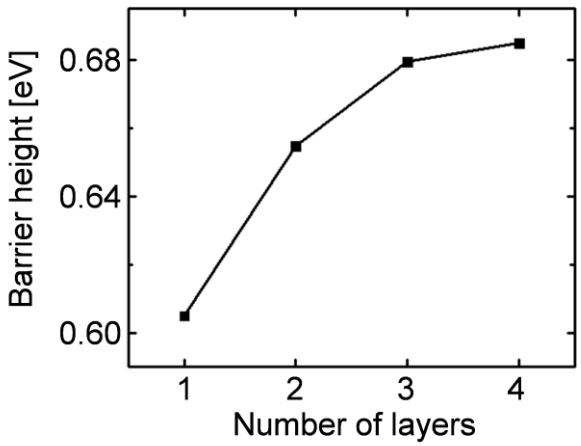

Figure S3. A plot of barrier heights as a function of MoS_2 layer number.

4. Additional conductive AFM (C-AFM) images in dark

The following are additional current maps in the dark that were not shown in Figure 2 in the main text.

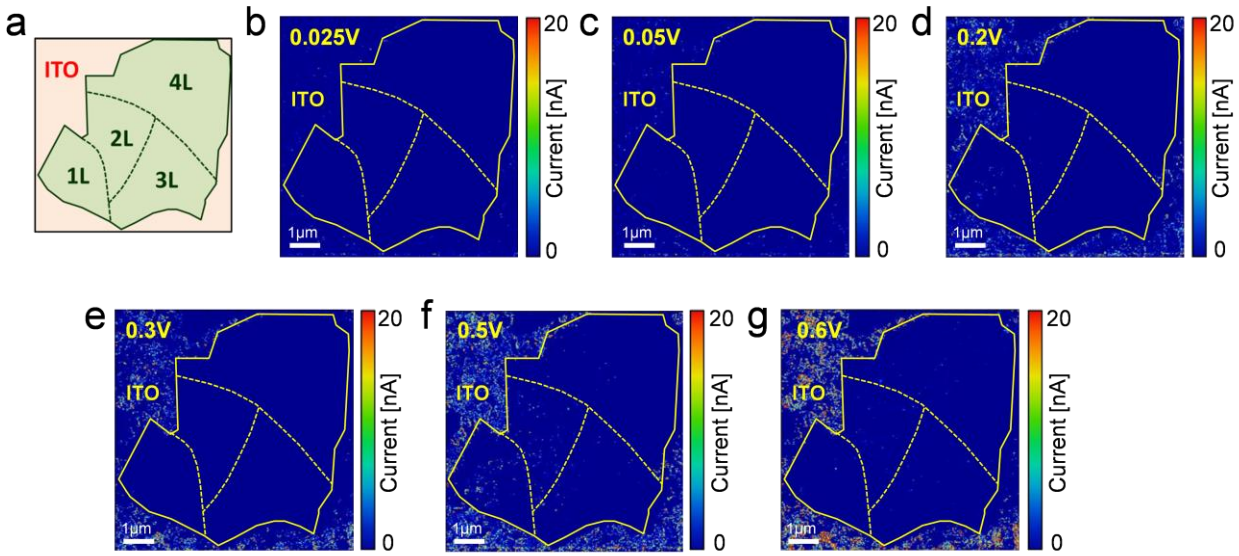

Figure S4. Additional C-AFM images in dark. (a) Schematic illustration of the MoS_2 nanosheet, indicating the regions of different layer numbers. (b)-(g) Current maps generated by conductive AFM measurements in the dark under applied sample bias voltages of (b) 0.025 V, (c) 0.05 V, (d) 0.2 V, (e) 0.3 V, (f) 0.5 V, and (g) 0.6 V.

5. Additional sample characterization and C-AFM images

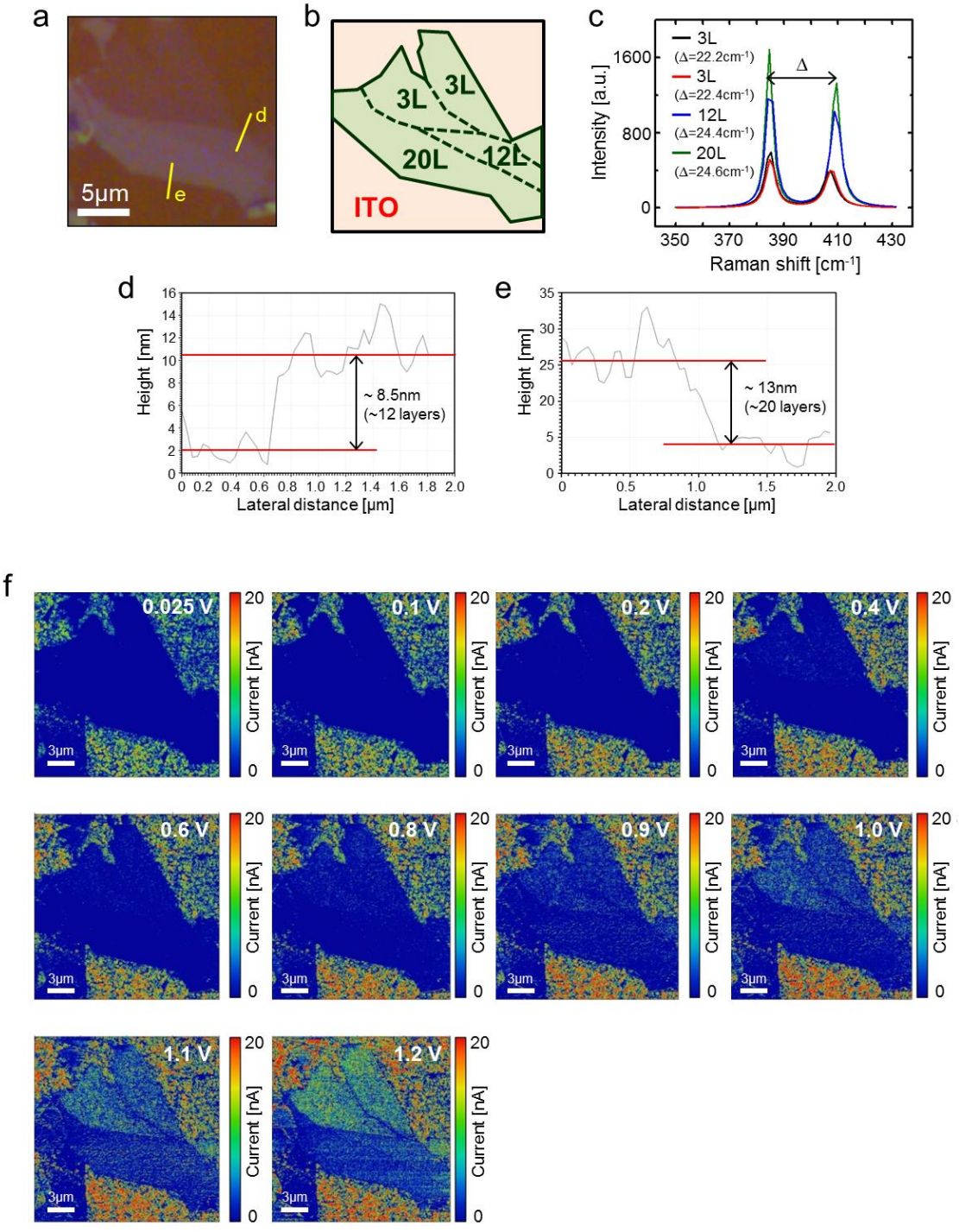

Figure S5. Additional Raman characterization, optical and C-AFM images in the dark. (a) An optical image of a MoS_2 crystal that consists of 3, 12 and 20-layer subregions deposited on ITO surface. (b) Schematic illustration of the MoS_2 nanosheet, indicating the regions of different layer numbers. (c) Representative Raman spectra taken at each region where the signature peak difference (Δ) was obtained to be 22.2, 22.4, 24.8 and 25.0 cm^{-1} for 3L, 3L, 12L and 20L, respectively. (d, e) A cross-sectional plot along the yellow line in (b) labelled as d and e, respectively. (f) Current maps taken by conductive AFM measurements under applied sample bias voltages of (b) 0.025V, 0.1V, 0.2V, 0.4V, 0.6V, 0.8V, 0.9V, 1.0V, 1.1V, and 1.2V.

6. Additional photoresponse map of MoS_2 nanosheet under illumination of λ = 800 nm

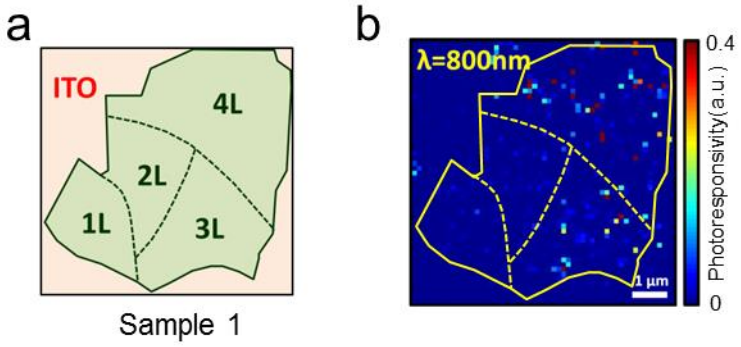

Figure S6. (a) A topographical sketch of the sample for visual guide. (b) An additional photoresponse map of MoS_2 nanosheet under illumination of λ = 800 nm by subtracting dark current images from that obtained under laser which is further normalized by the incident laser power.

7. Additional photocurrent spectral atomic force microscopy (PCS-AFM) images

The following are current maps in the dark and with illumination that were used to generate the spectral photoresponse maps presented in Figures 3b-f in the main text.

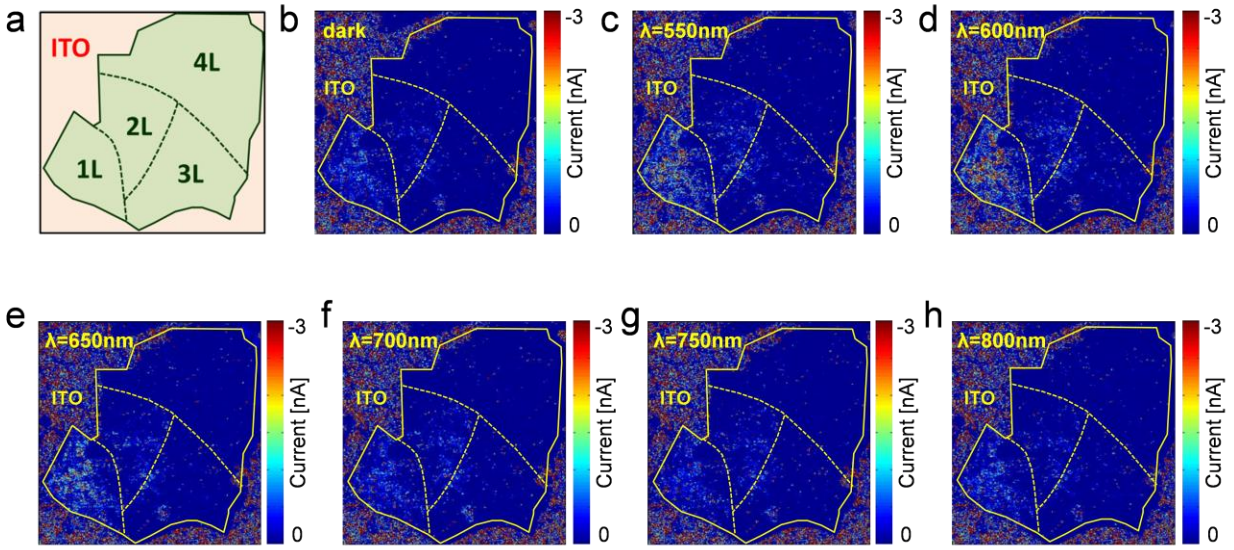

Figure S7. Current images under illumination. (a) Schematic illustration of the MoS_2 nanosheet, indicating the regions of different layer numbers. (b)-(h) Current maps generated by conductive AFM measurements (b) in the dark and under laser illumination of (c) λ = 550 nm, (d) 600 nm, (e) 650 nm, (f) 700 nm, (g) 740nm, and (h) 800 nm with an applied sample bias voltage of -0.6 V.

S8: Additional sample characterization and PCS-AFM images

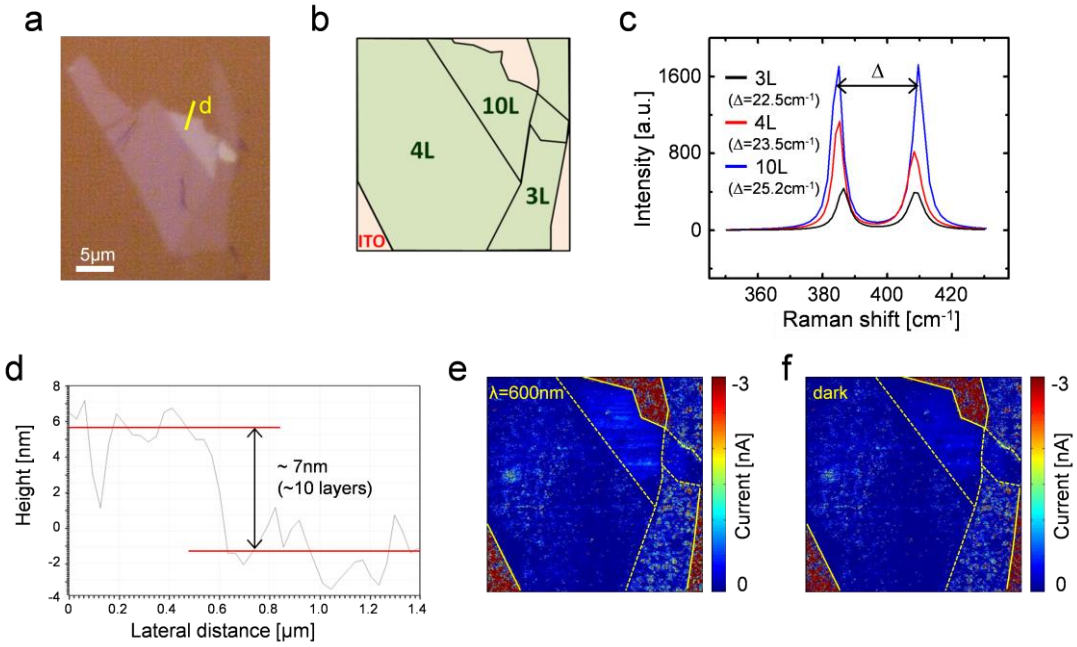

Figure S8. Additional Raman characterization, optical and C-AFM images in the dark. (a) An optical image of an MoS2 crystal that consists of 3, 4 and 10-layer subregions deposited on ITO surface. (b) Schematic illustration of the MoS_2, indicating the regions of different layer numbers. (c) Representative Raman spectra taken at each region where the signature peak difference (Δ) was obtained to be 22.5, 23.5 and 25.2 cm^{-1} for 3L, 4L, and 10L, respectively. (d) A cross-sectional plot along the yellow line in (a) labelled as d. (e-f) Current maps generated by conductive AFM measurements (e) under laser illumination of (c) λ = 600 nm and (f) in the dark with an applied sample bias voltage of -0.6 V that were used for generating the photoresponse map presented in Figure 3i in the main text.

S9: Additional PCS-AFM images for dependence of photoconductivity on bias voltage

The following are additional photoresponse maps under different bias voltages applied under laser illumination of λ = 600 nm that were not shown in Figure 4 in the main text, and current maps in the dark and with illumination that were used to generate the photoresponse maps shown in Figures 4b-g and S8a with varying voltages applied.

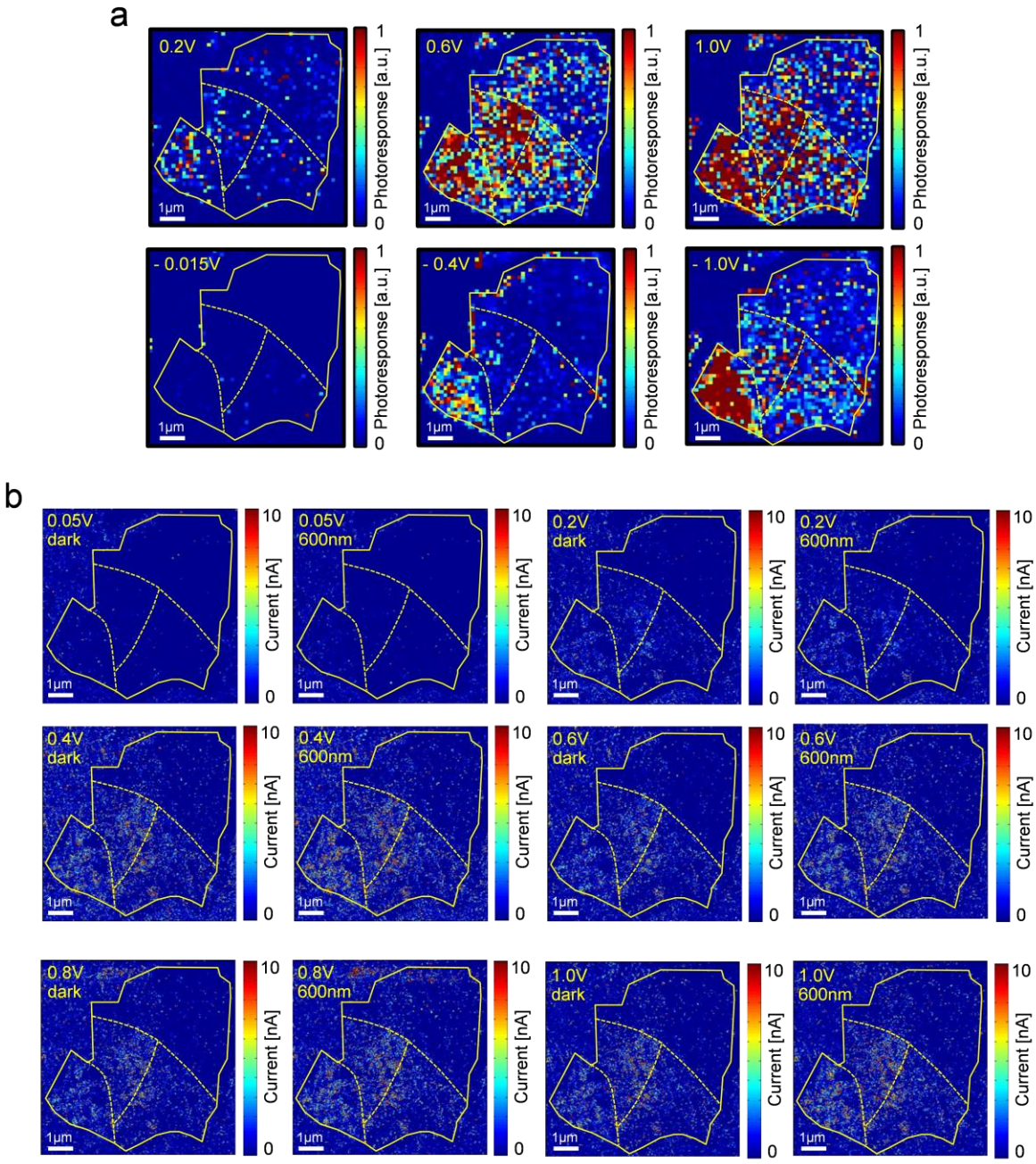

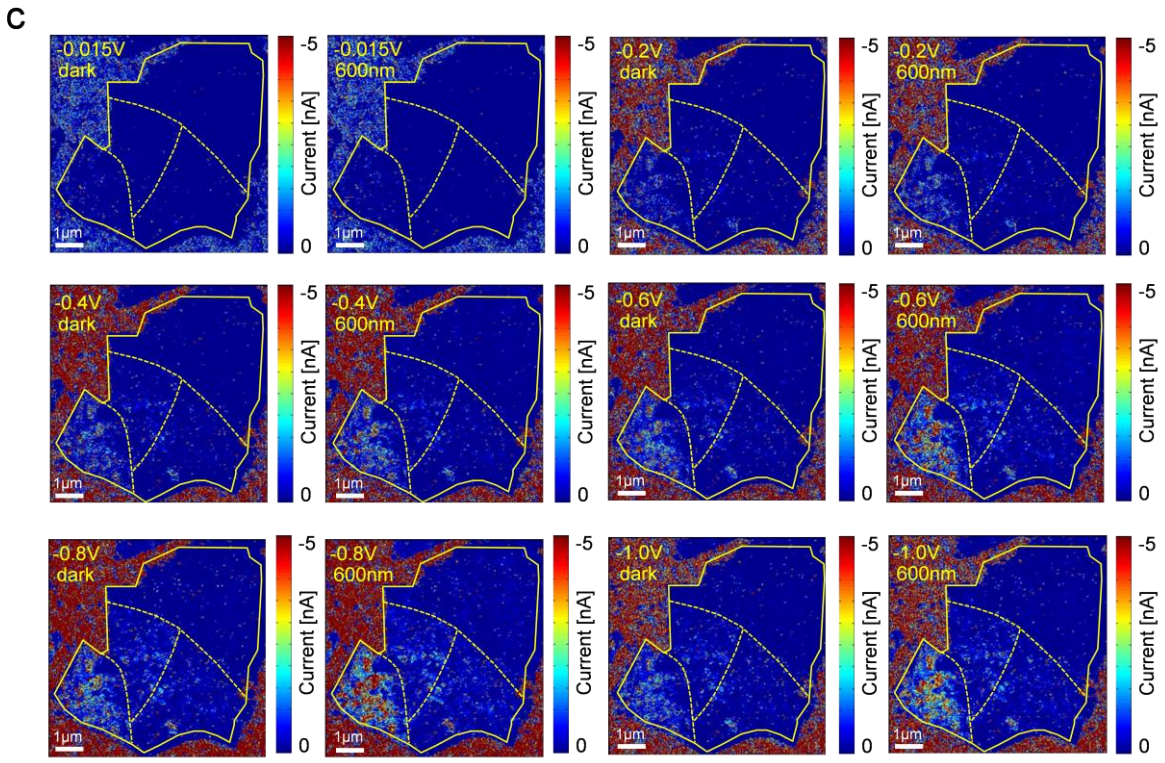

Figure S9. Dependence of photoconductivity on bias voltage and incident laser power. (a) Photoresponse maps of the MoS_2 flake at forward bias voltages of 0.2 V, 0.6 V, and 1.0 V, and reverse bias voltages of -0.015 V, -0.4 V, and -1.0 V under illumination of λ = 600 nm. (b-c) Current maps generated by PCS-AFM measurements under laser illumination of λ = 600 nm and in the dark with an applied (b) forward and (c) reverse bias voltage applied that were used to generate the photoresponse maps presented in Figures 4b-g and S8a.

10. Dependence of photoconductivity on different incident laser power

The following are photocurrent maps under different incident laser power density (λ = 550 nm) and PCS-AFM images used to generate the photocurrent maps that were not presented in the main text.

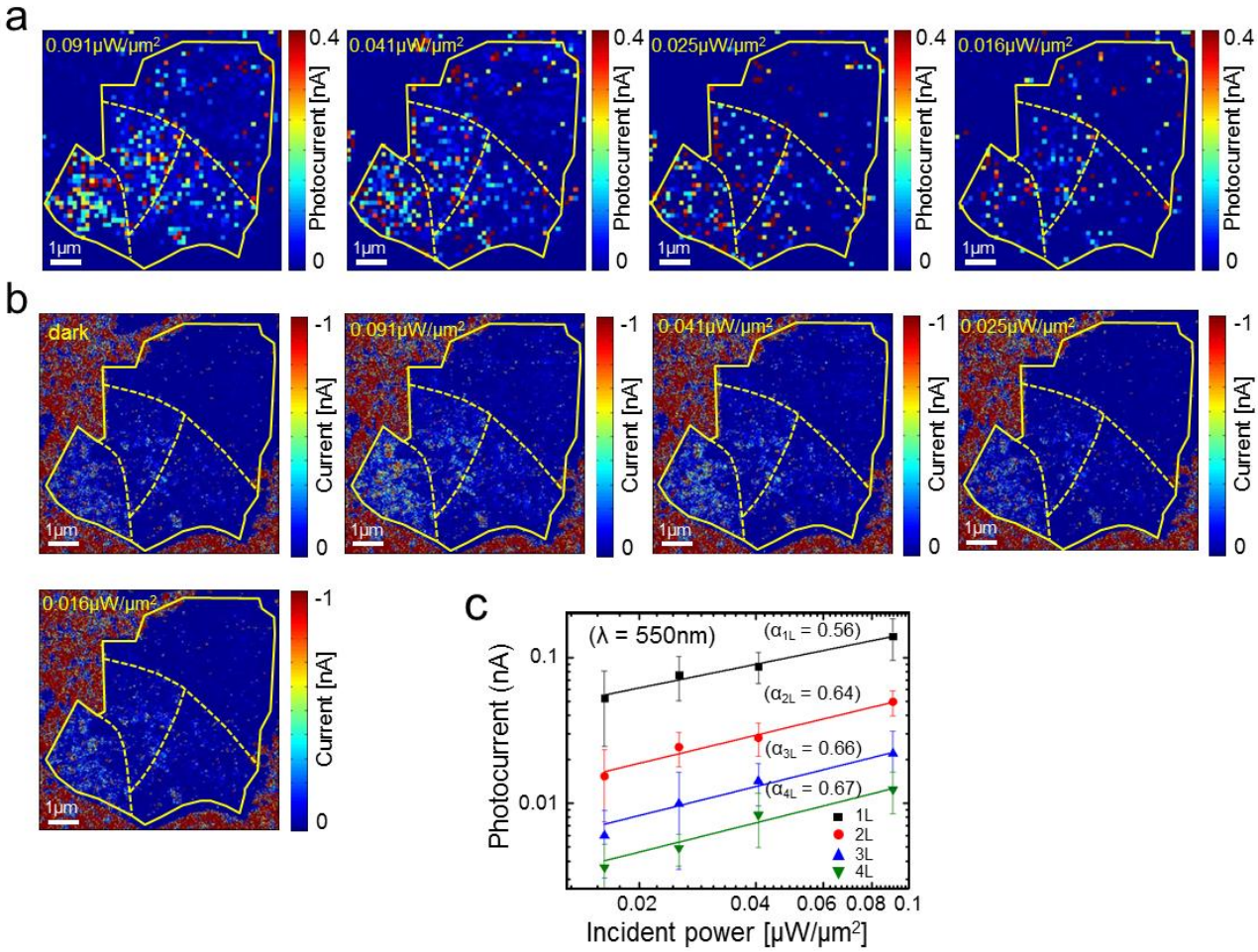

Figure S10. Dependence of photoconductivity on incident laser power. (a) Photocurrent maps under varying incident laser power density of 0.091μW/ μm^2, 0.041μW/ μm^2, 0.025μW/ μm^2, and 0.016μW/ μm^2 (λ = 550 nm). (b) Current maps generated by PCS-AFM under varying incident laser power density of 0.091μW/ μm^2, 0.041μW/ μm^2, 0.025μW/ μm^2, and 0.016μW/ μm^2 with an applied bias of -0.6V that were used to generate the photocurrent maps shown in (a). (c) Log-log plot of photocurrent as a function

of incident laser power density where straight lines are fit to the power law. A sublinear dependence on the incident laser intensity is observed, where power exponents range from 0.56 to 0.67.

References

1. Cappella, B.; Dietler, G. Force-Distance Curves by Atomic Force Microscopy. *Surf. Sci. Rep.* 1999, 34, 1-104.
2. Frammelsberger, W.; Benstetter, G.; Kiely, J.; Stamp, R. C-AFM-Based Thickness Determination of Thin and Ultra-Thin SiO2 Films by Use of Different Conductive-Coated Probe Tips. *Appl. Surf. Sci.* 2007, 253, 3615-3626.
3. Ruskell, T. G.; Workman, R. K.; Chen, D.; Sarid, D.; Dahl, S.; Gilbert, S. High Resolution Fowler-Nordheim Field Emission Maps of Thin Silicon Oxide Layers. *Appl. Phys. Lett.* 1996, 68, 93.
4. Teichert, C.; Beinik, I. Conductive Atomic-Force Microscopy Investigation of Nanostructures in Microelectronics. In *Scanning Probe Microscopy in Nanoscience and Nanotechnology 2*, Bhushan, B., Ed. Springer Berlin Heidelberg: 2011; pp 691-721.
5. Brandes, E. A.; Brook, G. B. Smithells Metals Reference Book, 7th ed.; Elsevier, 1998.
6. Castellanos-Gomez, A.; Poot, M.; Steele, G. A.; van der Zant, H. S. J.; Agraït, N.; Rubio-Bollinger, G. Elastic Properties of Freely Suspended MoS2 Nanosheets. *Adv. Mater.* 2012, 24, 772-775.
7. Lovell, M. R.; Khonsari, M. M.; Marangoni, R. D. A Finite Element Analysis of the Frictional Forces between a Cylindrical Bearing Element and MoS2 Coated and Uncoated Surfaces. *Wear* 1996, 194, 60-70.
8. Sze, S. M.; Ng, K. K. *Physics of Semiconductor Devices*. 3rd ed.; Wiley-Interscience: Hoboken, NJ, 2007